The effect of dynamic topography and gravity on lithospheric effective elastic thickness estimation: a case study

Yongliang Bai[a,b,*], Dongdong Dong[b], Jon F. Kirby[c], Simon E. Williams[d], Zhenjie Wang[a]

[a] School of Geosciences, China University of Petroleum, Qingdao 266580, China

[b] Key Laboratory of Marine Geology and Environment, Institute of Oceanology, Chinese Academy of Sciences, Qingdao 266071, China

[c] School of Earth and Planetary Sciences, Curtin University, WA 6845, Australia

[d] EarthByte Group, School of Geosciences, University of Sydney, NSW 2006, Australia

Abbreviated title: Improving T_e estimations by dynamic modelling

[*] Corresponding author, E-mail address: yongliang.bai1986@gmail.com (Y.Bai).

SUMMARY

Lithospheric effective elastic thickness (T_e), a proxy for plate strength, is helpful for the understanding of subduction characteristics. Affected by curvature, faulting and magma activity, lithospheric strength near trenches should be weakened but some regional inversion studies have shown much higher T_e values along some trenches than in their surroundings. In order to improve T_e estimation accuracy, here we discuss the long-wavelength effect of dynamic topography and gravity on T_e estimation by taking the Izu-Bonin-Mariana (IBM) Trench as a case study area. We estimate the long-wavelength influence of the density and negative buoyancy of the subducting slab on observed gravity anomalies and seafloor topography. The residual topography and gravity are used to map T_e using the fan-wavelet coherence method. Maps of T_e, both with and without the effects of dynamic topography and slab gravity anomaly, contain a band of high-T_e values along the IBM Trench, though these values and their errors are lower when slab effects are accounted for. Nevertheless, tests show that the T_e map is relatively insensitive to the choice of slab-density modelling method, even though the dynamic topography and slab-induced gravity anomaly vary considerably when the slab density is modelled by different methods. The continued presence of a high-T_e band along the trench after application of dynamic corrections shows that, before using 2D inversion methods to estimate Te variations in subduction zones, there are other factors that should be considered besides the slab dynamic effects on the overriding plate.

Key words: effective elastic thickness; lithospheric strength; Izu-Bonin-Mariana subduction system; slab density; dynamic topography; slab gravity anomaly

1 INTRODUCTION

The physical properties of the lithosphere govern intra-plate convergence and inner-plate deformation and therefore exert a strong control on trench shape and back-arc spreading (Forsyth and Uyeda, 1975; Niu, 2014). One of the most important of these physical properties is the flexural rigidity, which is a measure of the lithosphere's resistance to bending under applied loads, whether from above, below or within (Burov and Diament, 1995; Watts et al., 1980). The effective elastic thickness (T_e), a quantity which can be estimated from the coherence between topography and Bouguer gravity anomaly, is related to lithospheric flexural rigidity (McKenzie and Fairhead, 1997) and its rheological structure (Oruç and Sönmez, 2017). Available gravity and topography/bathymetry data can be used to compute lateral variations of T_e, and therefore study the geodynamic characteristics of a region, including subduction zones. For example, Pérez-Gussinyé et al. (2008) estimated the geodynamic relationship between subduction geometry and lithospheric strength along the Andean margin by estimating effective elastic thickness based on the Bouguer coherence technique, while Ratheesh Kumar et al. (2013) evaluated the convergence characteristics of subduction along the Indonesian active continental margin, also by estimating T_e from the Bouguer coherence.

Oceanic plate strength is strongly related to its temperature structure (Kalnins and Watts, 2009) because thermal softening induced by magmatic activity reduces lithospheric strength (Ebinger et al., 1989). The existence of present-day back-arc spreading, and active magmatic arcs and forearcs across the Izu-Bonin-Mariana (IBM,

Figure 1) arc region (Stern et al., 2004) demonstrates that there exists considerable magmatic activity. Hence, the lithosphere of the IBM regions surrounded by arcs should be weak. The downward bending of the incoming plate by subduction introduces significant fracturing and so reduces the strength of the incoming plate near trench (Bry and White, 2007; McNutt and Menard, 1982). Therefore, the lithosphere at the trench and neighboring regions should have a reduced T_e value. Indeed, studies using forward and inverse modelling of one-dimensional (1D) gravity/bathymetry profiles along the IBM subduction zone found reduced T_e values (Billen and Gurnis, 2005; Bry and White, 2007; Contreras-Reyes and Osses, 2010; Hunter and Watts, 2016; Zhang et al., 2014). However, 2D T_e-estimation methods have shown a band along the IBM Trench with obviously higher T_e values than the surroundings (Chen et al., 2013; Kalnins and Watts, 2009).

Along the Andean margin, the effects of slab gravity and dynamic topography on estimated T_e values are negligible (Pérez-Gussinyé et al., 2008). The subducting Nazca plate (younger than 50 m.y.) has a relatively small slab density contrast with the mantle and a small sinking force, resulting in a small slab gravity anomaly and dynamic topography. However, the IBM trench sees the subduction of the oldest oceanic plate (older than 130 m.y.) on the Earth and is under strong back-arc spreading (Stern et al., 2004). Therefore, the effects of dynamic topography and slab gravity along the IBM Trench are, in contrast, non-negligible for T_e studies. Here we estimate these effects on T_e estimations based on different slab density modelling methods.

2 METHODOLOGY

The effective elastic thickness (T_e) is related to the lithosphere's flexural rigidity (D) by:

$$D = \frac{ET_e^3}{12(1-\nu^2)}, \quad (1)$$

where E is Young's modulus, ν is Poisson's ratio, and both E and ν can be treated as constants (Walcott, 1970). Under long-wavelength loading, the lithosphere is isostatically compensated by a mechanism such as Airy isostasy, and the coherence between topography and Bouguer anomaly tends to a value of 1 (Chen et al., 2015; Pérez-Gussinyé et al., 2004). Short-wavelength loads that can be supported by lithospheric strength result in almost no lithospheric flexure, in which case the coherence between loading and Bouguer anomaly tends to zero (Forsyth, 1985; Pérez-Gussinyé et al., 2004). Simons and Olhede (2013) give an expression for the coherence transition wavelength, being the wavelength separating compensated from supported loads, and at which the coherence has a value of 0.5. A related expression is provided by the flexural wavelength (λ), being the wavelength of the depression due to a point surface load, and related to T_e (Macario et al., 1995):

$$\lambda = 2\pi\left(\frac{ET_e^3}{12(1-\nu^2)} / \Delta\rho \, g\right)^{1/4}, \quad (2)$$

where $\Delta\rho$ is the density contrast across the compensation surface (usually taken to be the Moho), and g is the acceleration due to gravity. Although the coherence transition and flexural wavelengths are of the same order of magnitude, they do differ for very high or very low values of the initial subsurface-to-surface loading ratio (Kirby and Swain, 2008).

2.1 T_e estimation using fan wavelet

There are two main widely-used methods for mapping spatial variations in T_e based on the coherence between the Bouguer gravity anomaly and topography/bathymetry: the multitaper (McKenzie and Fairhead, 1997; Simons et al., 2000) and the fan wavelet coherence method (Kirby, 2005; Kirby and Swain, 2004). The multitaper method uses a moving window of fixed dimensions to obtain spatially varying coherence values across an area and from this constructs a T_e map. The need to select a window size limits the multitaper method in two ways: firstly, flexure cannot be resolved when the window size is smaller than the flexural wavelength; secondly, a large window size cannot image detailed spatial variations in T_e (Chen et al., 2013; Kalnins and Watts, 2009; Pérez-Gussinyé et al., 2008; Pérez-Gussinyé et al., 2004). The fan wavelet method avoids these shortcomings, so we choose this method to estimate T_e distribution in our research area. Nevertheless the fan wavelet method faces the problem that the resolution of the T_e map depends on the central wavenumber (CW) of the Morlet wavelet used in the wavelet analysis (Chen et al., 2015; Kirby, 2014).

Kirby and Swain (2004) constructed the fan wavelet by superposition of a series of rotated Morlet wavelets, giving isotropic and complex wavelet coefficients. The Fourier transform of the two dimensional (2D) Morlet wavelet is

$$\hat{\psi}_{s\theta}(\mathbf{k}) = s e^{-\left[(su-|k_0|\cos\theta)^2+(sv-|k_0|\sin\theta)^2\right]/2}, \tag{3}$$

where $|\mathbf{k}_0|$ is the central wavenumber (CW), u and v are the components of the 2D wavenumber vector $\mathbf{k}$, s is the scale of the wavelet, and θ is its azimuth. Each Morlet wavelet scale is related to an equivalent Fourier wavenumber, k_F, by $k_F = |\mathbf{k}_0|/s$ (Kirby, 2005).

The wavelet transform is a space-domain convolution between the signal to be analyzed and the wavelet. This convolution is performed at all the selected scales and azimuths, and as such, reveals the harmonic content of the signal at each space-domain grid node and azimuth. The wavelet transform is most efficiently performed in the wavenumber domain where convolution becomes multiplication, yielding wavelet coefficients $B_{s\mathbf{x}\theta}$ via the equation:

$$B_{s\mathbf{x}\theta} \equiv B(s,\mathbf{x},\theta) = \mathbf{F}^{-1}\left[\hat{b}(\mathbf{k})\,\hat{\psi}_{s\theta}(\mathbf{k})\right], \tag{4}$$

where $\mathbf{F}^{-1}$ is the inverse 2D Fourier transform operator, and $\hat{b}(\mathbf{k})$ is the Fourier transform of the space domain signal $b(\mathbf{x})$.

The 2D observed wavelet coherence ($\gamma^2_{obs}(s,\mathbf{x})$) between observed Bouguer gravity anomaly and topography at scale (s) and location ($\mathbf{x}$) is calculated by summing the wavelet cross- and co-spectra over azimuth (Kirby and Swain, 2008; Kirby and Swain, 2011):

$$\gamma^2_{obs}(s,\mathbf{x}) = \frac{\left|\left\langle B_{s\mathbf{x}\theta} H^*_{s\mathbf{x}\theta}\right\rangle_\theta\right|^2}{\left\langle B_{s\mathbf{x}\theta} B^*_{s\mathbf{x}\theta}\right\rangle_\theta \left\langle H_{s\mathbf{x}\theta} H^*_{s\mathbf{x}\theta}\right\rangle_\theta}, \tag{5}$$

where $B_{s\mathbf{x}\theta}$ and $H_{s\mathbf{x}\theta}$ are the complex wavelet coefficients of Bouguer anomaly and topography, respectively, the * indicates the complex conjugate, and $\langle\ \rangle_\theta$ represents averaging over Morlet wavelet azimuth.

The observed coherence is then inverted against the predictions of a thin, elastic plate model of plate flexure using the wavelet adaptation of the method of Forsyth (1985) by Swain and Kirby (2006). The inversion for T_e is performed by comparing the observed coherence with the predicted coherence at each space-domain grid node, where the predicted coherence can be computed by (Chen et al., 2015; Kirby and Swain, 2011)

$$\gamma_{pre}^2(s,\mathbf{x}) = \frac{(\mu_T\kappa_T + \mu_B\kappa_B f^2 r^2)^2}{(\mu_T^2 + \mu_B^2 f^2 r^2)(\kappa_T^2 + \kappa_B^2 f^2 r^2)}. \tag{6}$$

Here, f is the subsurface to surface loading ratio which can be determined by:

$$f^2(s,\mathbf{x}) = \frac{\left\langle |W_i|^2 \right\rangle_\theta}{r^2 \left\langle |H_i|^2 \right\rangle_\theta}, \tag{7}$$

where W_i and H_i are the wavelet coefficients of initial surface and subsurface loads which are assumed to be statistically independent (have random phase) (Forsyth, 1985) and are products of the inversion (Forsyth, 1985; Swain and Kirby, 2006). Other variables used in equation (6) are calculated from:

$$\begin{cases} \kappa_B = \Delta\rho_2 / \varphi \\ \kappa_T = 1 - \Delta\rho_1 / \varphi \\ \mu_B = 2\pi G \Delta\rho_2 (1 - \Delta\rho_2 / \varphi) e^{-kZ_m} \\ \mu_T = 2\pi G \Delta\rho_2 (-\Delta\rho_1 / \varphi) e^{-kZ_m} \\ \varphi = Dk^4 / g + (\rho_m - \rho_w) \end{cases}, \tag{8}$$

where $\Delta\rho_1 = \rho_b - \rho_*$, $\Delta\rho_2 = \rho_m - \rho_b$; $r = \Delta\rho_1 / \Delta\rho_2$; ρ_* is seawater or air density depending on the setting (continent or ocean); ρ_m, ρ_b and ρ_w are densities of mantle, basement and seawater respectively; Z_m is the depth to the compensating interface (the Moho); g is the gravitational acceleration, G is the Newtonian gravitational constant; and $k \equiv |\mathbf{k}|$ is the 1D wavenumber which can be replaced by the equivalent Fourier wavenumber in the fan wavelet case (Kirby, 2005).

The T_e value at each grid node is obtained by minimizing the misfit between predicted and observed coherence (Chen et al., 2015; Kirby and Swain, 2011). Since the final T_e resolution would be affected by central wavenumber values, we compute T_e maps based on four different $|\mathbf{k}_0|$ values (2.668, 3.081, 3.773 and 5.336) as done by Chen et al. (2015). See Kirby and Swain (2011) for an explanation of the $|\mathbf{k}_0|$ values. The values of the constants used for estimating T_e are shown in Table 1.

Error estimates on the coherence were obtained using the jackknife method of error estimation (Thomson and Chave, 1991) applied to wavelets (Kirby and Swain, 2013). The coherence errors were then used as weights on the difference between observed and predicted coherence in minimization of the square of the L_2-norm (chi-squared statistic) (Kirby, 2014). Errors on T_e were obtained from the width of the misfit curve in the parameter space (where T_e is the only parameter) corresponding to a confidence level of 95% (Press et al., 1992).

Kirby and Swain (2008, 2011) have performed extensive tests on the accuracy of the method under different scenarios using synthetic, fractal loading models. Results have been encouraging. Of particular note here is the test on a plate with a T_e discontinuity, representing a fault or subduction zone (Kirby and Swain, 2008).

2.2 Dynamic topography and slab gravity anomaly

Loading of lithosphere is a key parameter for T_e evaluations and loading is not limited to topographic variations. Figure 2 illustrates factors which include surface loading such as mountains and seawater, and internal loading such as high-density magmatic intrusions into the basement and dynamic forces from beneath the lithosphere (Bry and White, 2007), referred to as under-loading in this paper. Here we convert the bathymetry to a rock-equivalent topography:

$$h_{eq}(\mathbf{x}) = \frac{\rho_c - \rho_w}{\rho_c} d(\mathbf{x}), \quad \forall d(\mathbf{x}) < 0 \tag{9}$$

where $d(\mathbf{x})$ is the bathymetry or topography at location $\mathbf{x}$ and $h_{eq}(\mathbf{x})$ is the equivalent topography at the same position. A similar conversion also should be used to calculate the equivalent topography of sediment cover when it is thick (Shi et al., 2017):

$$h_{eq}(\mathbf{x}) = \frac{\rho_c - \rho_s}{\rho_c} d(\mathbf{x}), \quad \forall d(\mathbf{x}) < 0. \tag{10}$$

Where ρ_s is sediment density and $d(\mathbf{x})$ is sediment thickness. Since it is hard to accurately constrain the detailed basement density distribution, we will assume that basement density in the research area is uniform.

There also exists a downward pulling force on the overlying lithosphere caused by the sinking of the subducted slab and transmitted by the asthenospheric wedge (Flament et al., 2013; Gvirtzman et al., 2016; Husson, 2006). The topography changes induced by this slab dynamic force are called 'dynamic topography' in this paper; the variation of this topography is predominantly long wavelength. The density contrast between the subducting slab and the mantle also causes a long-wavelength gravity perturbation, with this gravity anomaly referred to as 'dynamic gravity' or 'slab gravity anomaly' in this paper.

To evaluate the long-wavelength downward pulling force on the overlying lithosphere by slab sinking, the sinking slab is separated into discrete elements. Based on the Stokes stream function, the pulling force (*F*) on a lithospheric surface point can be calculated by (Husson, 2006; Morgan, 1965):

$$F = \frac{3\Delta\rho_{ij} v_{ij} g z_{ij}^3}{\pi r_{ij}^5}, \tag{11}$$

where i, j is the slab element index, $\Delta\rho_{ij}$ is the density difference between this slab unit and the background mantle, v_{ij} is the volume of the unit, g is the gravitational acceleration, z_{ij} is the depth of the unit and r_{ij} is the distance between the slab unit and the surface point. The overlying lithosphere will be bent downward, so when the surface deflection is *h* then the buoyancy force change of the overlying lithosphere induced by this deflection is:

$$\sigma = (\rho_m - \rho_*) g h, \tag{12}$$

where ρ_m is mantle density and ρ_* is seawater or air density. If it is a stress-free surface then the buoyancy force change (σ) should be equal to the slab pulling force (F). Hence the total deflection (*H*) of the lithosphere surface point by the three-dimensional slab can be calculated by equating eqs (11) and (12) and summing over all elements:

$$H = \sum_j \sum_i \frac{3\Delta\rho_{ij} v_{ij} z_{ij}^3}{\pi r_{ij}^5 (\rho_m - \rho_*)}. \tag{13}$$

Except for the density perturbation of the slab unit ($\Delta\rho_{ij}$), all the other parameters can be assumed (Table 1) or calculated according to element coordinates.

Here we compare three methods for slab-density modelling. First, Deschamps et al. (2001) noted that both the lithosphere density (ρ) and seismic shear-wave velocity (Vs) are dependent on similar parameters, such as temperature, composition, pressure, etc.. This led Isaak et al. (1989) to derive a crude quantitative relationship between ρ and Vs when only temperature affects ρ and Vs:

$$\zeta = \frac{\ln \rho - \ln \rho_0}{\ln Vs - \ln Vs_0} \tag{14}$$

where the ratio (ζ) is 0.1 when depth is shallower than 400 km, and 0.2 when depth is between 400 km and 700 km, according to the study by Karato (1993). The parameters ρ_0 and Vs_0 are reference density and shear-wave velocity, respectively; we call this method “Isaak1989”. A second method for slab density modelling is based on laboratory data by Karato and Karki (2001) which assigns a constant velocity-density conversion factor of 0.15 cm^{-3} km^{-1} s; we call this method “KK2001”. The third method we consider assigns a slab density anomaly of 25 kg m^{-3} relative to its surroundings, as Pérez-Gussinyé et al. (2008) assumed; we call this “PG2008”.

After assuming slab thickness to be uniformly 100 km as Husson (2006) did, and extracting the shear-wave velocity of the subducted slab, the slab density perturbation can be derived from Vs data and equation (14) by taking the Earth model of Dziewonski and Anderson (1981) as reference. The dynamic topography due to the slab density perturbation can then be calculated using equation (13). Additionally, the dynamic gravity due to the slab density perturbation can be calculated in the frequency domain (Oldenburg, 1974; Parker, 1973). The topography and gravity after removal of the slab effects are called here the ‘residual’ topography and gravity, respectively.

3 CASE STUDY AT THE IBM SUBDUCTION ZONE

3.1 Geologic setting

Subduction of the Pacific plate under the West Philippine Sea plate began by ~52-45 Ma (Arculus et al., 2015; Stern et al., 2004) and this subduction resulted in the formation of the IBM Trench. The IBM subduction hinge roll back commenced with the opening of two back-arc basins, the Shikoku and Parece Vela Basins, in the Late Oligocene (Hall, 2002; Hilde et al., 1977; Honza and Fujioka, 2004). Part of the initial volcanic arc remains on the western margin of these basins as a linear bathymetric high named the Kyushu Palau Ridge (Figure 1). The seafloor spreading direction of the Shikoku Basin changed from ENE–WSW to NE–SW around 19 Ma; the Parece Vela Basin spreading direction changed around 20 Ma, from E-W to NE–SW, possibly related to rotation of the Philippine Sea plate (Hall, 1996; Sdrolias et al., 2004). These mid-ocean ridge spreading direction changes induced the formation of S-shaped fracture zones in these two basins (Sdrolias et al., 2004). Back-arc spreading in the Shikoku Basin and Parece Vela Basins ceased at ~15 Ma.

A hiatus in back-arc spreading then occurred in this area until the Mariana Trough’s initiation at ~7 Ma, which is still spreading at the back of the Mariana Trench (Jolivet et al., 1989). Continuous subduction after cessation of the Shikoku and Parece Vela Basin’s back-arc spreading resulted in widening of the Izu-Bonin-Mariana Arc. The previous Mariana Arc was split into two parts by the newly formed Marina

Trough which is bounded by the West Mariana Arc and East Mariana Arc (Figure 1).

The region of the subducting Pacific plate in our research area which is older than ~130 Ma (Müller et al., 2008) has cooled and subsided to great depths. Within this region, the subduction systems form deep trenches and contain the lowest point (the Challenger Deep) on the Earth's surface, at more than 10 km depth. The incoming western Pacific plate is much older and denser than the over-riding Shikoku and Parece Vela Basins (30 -15 Ma) (Sdrolias et al., 2004) and provides a large enough negative buoyancy to sustain subduction (Hall et al., 2003; Niu, 2014). The subduction process is, however, affected by the sea-bottom topography and density distribution of the incoming Pacific plate (Zhang et al., 2016). For example, the docking of Bonin (Ogasawara) Plateau (Figure 1b) which is about 2 km to 3 km higher than the surrounding seafloor has already modified the shape of the IBM Trench (Kong et al., 2018; Mason et al., 2010).

3.2 Data sets

Forsyth (1985) coherence method requires the use of Bouguer, rather than free air gravity anomalies, since the coherence between the former and the topography is much less dependent on the loading ratio and model parameters such as layer depths and densities than is the coherence between the latter and the topography (e.g., Kirby, 2014). The ETOPO1 model is used for the land topography and ocean bathymetry in this study (Amante and Eakins, 2009), with a 1 arc minute grid spacing. In marine areas, the ETOPO1 is the combination of bathymetry measured from ships, and bathymetry inverted from satellite altimetry data. The Bouguer anomaly grid by Bureau Gravimétrique International (Balmino et al., 2012) is derived from the EGM2008 Geopotential model and the ETOPO1 Global Relief model, and this Bouguer grid is with 2 arc minutes resolution. The EGM2008 model includes surface gravity measurements, satellite altimetry and gravimetry measurements. Since our research area has thick water but thin sediment coverage (Amante and Eakins, 2009; Divins, 2004), equivalent topography is computed only from the bathymetry using the seawater depth from ETOPO1. Global shear-wave velocity structure from surface to 700 km depth by Schaeffer and Lebedev (2013) is used for computing the dynamic topography and slab gravity anomaly. This velocity volume has a horizontal resolution of 0.5° and a vertical resolution of 25 km.

3.3 Elastic thickness results

We first computed the effective elastic thickness from the fan-wavelet method using the equivalent topography and Bouguer anomaly without the slab corrections. Four T_e maps were computed with four different central wavenumbers (CW, or $|\mathbf{k}_0|$). The T_e range for CW = 2.668 is 0.5 - 152.0 km, for CW = 3.081 it is 0.5 - 148.3 km, for CW = 3.773 it is 0.8 - 139.9 km, and for CW = 5.336 the range is 1.0 - 96.4 km. These initial results, before consideration of slab effects, are shown in Figure 3. Note the obvious high T_e band along, and to both sides of, the IBM Trench in each result.

The T_e map generated with the lowest central wavenumber (2.668) shows the most detail in the spatial variations of T_e (Figure 3a), while the 5.336 CW map (Figure

3d) is much longer-wavelength in nature due to such wavelets tending to smear information out over larger spatial scales (Kirby and Swain, 2011). It is this property of higher-CW wavelets, despite their superior wavenumber-domain resolution, that make them less suited for studies where T_e can change rapidly and by large amounts over short distances, as seems to be the case in this study area. To this end, we chose the smallest allowable value of $|\mathbf{k}_0|$, 2.668, in the following sections (which must be >2.5; Kirby and Swain, 2011).

Figure 4 shows the dynamic topography and gravity when the subducted slab's density structures are modelled with the PG2008, Isaak1989 and KK2001 methods, respectively. The dynamic topography and gravity results have a similar distribution but with reverse polarity because the positive density anomaly of the subducting slab induces a negative dynamic topography but positive gravity anomaly. Relatively large absolute dynamic topography and slab gravity anomaly values occur behind the trench, controlled by the density and position of the subducting slab (eq. (13)).

From the comparison between these three different groups of long-wavelength dynamic modelling results, we see that dynamic topography maps have a similar distribution trend but with different amplitudes. The smallest dynamic topography amplitude, with a value of 0.79 km, is based on the Isaak1989 method; the largest dynamic topography amplitude, with a value of 2.32 km, is based on the PG2008 method. The latter is almost three times the amplitude of the former. The dynamic gravity maps also have similar comparison characteristics. Therefore, different slab density modelling methods produce very different dynamic calculation results.

Slab effects on gravity and topography were removed from the Bouguer gravity anomaly and topography, giving residual quantities. The effective elastic thickness was then recomputed using the residual topography and gravity anomaly when CW = 2.668 (Figure 5). A comparison between T_e maps based on different slab density modelling methods (Figure 5) shows that these three T_e maps have very similar trends and similar amplitudes even though the dynamic topography and gravity vary considerably when the slab density modelling method changes. These three T_e maps also have very similar error distributions (Figure 6). Therefore, while dynamic topography and gravity values are relatively sensitive to slab density modelling, T_e estimations derived from them are not. The T_e values after application of the corrections are very much reduced, especially in the region surrounding the trench; this will be discussed in Section 3.5.

Figure 6 shows four T_e error maps before and after application of dynamic corrections to the gravity and topography data. The errors are uniformly low over the majority of the study area, while the largest errors are distributed along the high-T_e band surrounding the trench and on its boundary. The T_e estimations without dynamic corrections have the largest errors of the four; the mean value of this T_e error map (Figure 6a) is 2.7 km with a maximum error of 49.5 km. The mean T_e error after dynamic corrections when slab density is modelled based on the PG2008, Isaak 1989 and KK2001 methods, is reduced to 0.94 km, 0.93 km and 0.96 km, respectively, and the maximum error of each T_e map is 23.8 km, 21.0 km and 23.5 km, respectively. Therefore, both the mean and maximum values of T_e error have been considerably reduced by application of the dynamic corrections.

3.4 Comparison with previous studies

Two other studies have also mapped spatial variations of effective elastic thickness in this region (Chen et al., 2013; Kalnins and Watts, 2009). The T_e map by Chen et al. (2013) also used the Bouguer coherence method, though they used the multitaper method of spectral estimation, and used ETOPO2 for the topography/bathymetry data and free-air gravity anomalies from the EIGEN-6C model (http://icgem.gfz-potsdam.de/ICGEM/modelstab.html) to derive the Bouguer anomaly is; we call this study Chen2013. The T_e map by Kalnins and Watts (2009) used the free-air admittance method with a satellite altimetry-derived free-air gravity anomaly grid (V16.1) (Smith and Sandwell, 1994) and the GEBCO bathymetry grid (IOC, 2003); we refer to this map as KW2009. The western section of our research area coincides with the study area of Chen2013, while the eastern section coincides with that of KW2009.

There is no unusual T_e high along the Nankai Trough either in the Chen2013 map or in our T_e map (Figure 7b). Our average T_e value of Parece Vela Basin is 5.6 km and for the Shikoku Basin is 3.1 km (Figure 7b). Chen2013 also shows that the Parece Vela Basin has a stronger lithosphere than the Shikoku Basin. The T_e value of KW2009 for the incoming Pacific plate in the overlapping area between our model and KW2009 has a range of 0 - 15 km; our model has a similar range.

Both KW2009 and Chen2013 both have a very similar high-T_e band along the

IBM Trench, and neither considered the effect of dynamic topography and gravity by the subducting slab. The spatial distribution of our high-T_e band (Figure 7b) matches their geometries even though our methodology and input data are different from KW2009 and Chen2013. T_e maps from all studies have a sharp T_e transition on the boundaries of the high-T_e band. The T_e value along this band in Chen2013 is larger than 60 km which is similar to our first-step result (Figure 7a). The T_e values along this band in KW2009 lie between 25 - 50 km, a relatively small range compared to Chen2013, but still much larger than the surrounding T_e values. Our peak value in the region overlapping with KW2009 is 37.2 km. These observations demonstrate that, irrespective of which spectral analysis method is used (multitaper (Chen2013 and KW2009) or wavelet (our model)), high-T_e values along the IBM Trench are the outcome. But as noted above, removal of dynamic topography and gravity from the bathymetry/topography and gravity reduces the amplitude of this high-T_e band.

3.5 Influence of dynamic correction on T_e evaluation

Both faulting and magmatic activity reduce lithospheric strength (Billen and Gurnis, 2005; Bry and White, 2007; Chen et al., 2013; McNutt and Menard, 1982; Zhang et al., 2014). Therefore, one would expect T_e at the trench and its surrounding areas to have relatively small values. This is not seen in the T_e maps computed before corrections of the gravity and topography data (Figure 3).

The mean value of the high-T_e band bounded by black solid lines in Figure 7a is 76.7 km; the removal of slab effects from the data reduces the mean value within this high-T_e band by 56.9 km to 19.8 km (Figure 7b). Another difference between these two T_e maps (Figure 7a and Figure 7b) is that the boundaries between the high-T_e band and the adjacent regions are sharper in Figure 7a than in Figure 7b. Similar characteristics appear on the T_e error map (Figure 6). The high-T_e band of Figure 7a is much wider than the high-T_e band of Figure 7b. Reduction of the amplitude and width of the high-T_e band has brought the T_e value closer to the expectations of a curved, heated and faulted plate. This means that the dynamic correction could improve T_e estimation results along oceanic trenches.

3.6 Other possible influencing factors on T_e evaluation

The presence of a high-T_e band after dynamic corrections were made (Figure 5) illustrates that there are still some other factors affecting T_e estimates. Besides slab sinking, the surrounding mantle flow and density variations could also modify topography and gravity as shown in Figure 2, and thus could affect T_e estimates. But because the density and velocity of the upper mantle are affected not only by temperature but also by composition variations, it is difficult to image density distributions from seismic tomography. Therefore, density contrasts in the upper-most mantle have been ignored for dynamic studies (Conrad and Husson, 2009; Heine et al., 2008; Steinberger, 2007). The bottom depth of this section varies between different studies, for example, 220 km by Steinberger (2007) and Heine et al. (2008), and 300 km by Conrad and Husson (2009). Figure 8 shows that the mantle wedge has a clear low seismic velocity, but the mantle under the slab has a relatively uniform structure and small changes in velocity. These uncertainties provide the reason why we only consider slab dynamic effects.

Oceanic trenches and back-arc basins over a subducting slab are dynamically compensated by viscous mantle flow due to the force on the overriding plate induced by slab sinking and mantle wedge flow (Zhong and Gurnis, 1994). Stresses induced by slab sinking are transmitted along the slab to the surface, resulting in trench deepening, so the trench topography is compensated by the subducted slab (Davies, 1981). In this case, the compensation surface is not the Moho as supposed by the 2D T_e inversion method. Thus, T_e estimates along the trench based on 2D inversion would be biased. Therefore, before estimating T_e variations in subduction zones, other factors should be considered besides the slab dynamic effects on the overriding plate.

4 CONCLUSIONS

In this paper, we have attempted to study the effect of long-wavelength dynamic topography and gravity upon lithospheric effective elastic thickness estimation by taking the Izu-Bonin-Mariana Trench as a case study region. Dynamic topography and slab gravity anomaly induced by the subducted slab was estimated and then removed from the topography and gravity anomaly. The resulting residual topography and gravity anomaly were used to generate a T_e map using the fan wavelet coherence method. T_e maps generated before the removal of dynamic topography and slab gravity anomaly, and also the results of other studies (Chen et al., 2013; Kalnins and Watts, 2009), reveal a high-T_e band along and surrounding the IBM Trench, in disagreement with expectations of reduced T_e due to heating, faulting and plate curvature. However when the long-wavelength dynamic effects are applied, the amplitude and width of this high-T_e band is strongly reduced, in keeping with expectations. Our tests show that effective elastic thickness estimation results are relatively insensitive to the particular method of slab-density estimation, despite the model topography and gravity being more sensitive to model choice. The continued presence of a high-T_e band along the trench after application of dynamic corrections shows that, before using 2D inversion methods to estimate Te variations in subduction zones, there are other factors that should be considered besides the slab dynamic effects on the overriding plate.

ACKNOWLEDGMENTS

The authors thank the constructive comments and suggestions from two anonymous reviewers. This work is supported by National Natural Science Foundation of China (Grant No.41506055 and No.41476042), Open Fund of the Key Laboratory of Marine Geology and Environment CAS (MGE2017KG01), the Fundamental Research Funds for the Central Universities (No.17CX02003A) and Key Research Program of the Chinese Academy of Sciences (Grant No.Y10131).

REFERENCES

Amante, C., Eakins, B.W., 2009. ETOPO1 1 Arc-Minute Global Relief Model: Procedures, Data Sources and Analysis, in: NGDC-24, N.T.M.N. (Ed.). National

Geophysical Data Center, NOAA.

Arculus, R.J., et al., 2015. A record of spontaneous subduction initiation in the Izu-Bonin-Mariana arc. Nature Geosci 8, 728-733.

Balmino, G., et al., 2012. Spherical harmonic modelling to ultra-high degree of Bouguer and isostatic anomalies. Journal of Geodesy 86, 499-520.

Billen, M.I., Gurnis, M., 2005. Constraints on subducting plate strength within the Kermadec trench. Journal of Geophysical Research: Solid Earth 110, B05407.

Bry, M., White, N., 2007. Reappraising elastic thickness variation at oceanic trenches. Journal of Geophysical Research: Solid Earth 112, B08414.

Burov, E.B., Diament, M., 1995. The effective elastic thickness (Te) of continental lithosphere: What does it really mean? Journal of Geophysical Research: Solid Earth 100, 3905-3927.

Chen, B., et al., 2013. Variations of the effective elastic thickness over China and surroundings and their relation to the lithosphere dynamics. Earth and Planetary Science Letters 363, 61–72.

Chen, B., et al., 2015. Elastic thickness of the Himalayan–Tibetan orogen estimated from the fan wavelet coherence method, and its implications for lithospheric structure. Earth and Planetary Science Letters 409, 1-14.

Conrad, C.P., Husson, L., 2009. Influence of dynamic topography on sea level and its rate of change. Lithosphere 1, 110-120.

Contreras-Reyes, E., Osses, A., 2010. Lithospheric flexure modelling seaward of the Chile trench: implications for oceanic plate weakening in the Trench Outer Rise region. Geophysical Journal International 182, 97-112.

Davies, G.F., 1981. Regional compensation of subducted lithosphere: effects on geoid, gravity and topography from a preliminary model. Earth and Planetary Science Letters 54, 431-441.

Deschamps, F., et al., 2001. The relative density-to-shear velocity scaling in the uppermost mantle. Physics of the Earth and Planetary Interiors 124, 193-212.

Divins, D.L., 2004. Total Sediment Thickness of the World's Oceans & Marginal Seas, in: Center, N.N.G.D. (Ed.), Boulder, Colo.

Dziewonski, A.M., Anderson, D.L., 1981. Preliminary reference Earth model. Physics of the Earth and Planetary Interiors 25, 297-356.

Ebinger, C.J., et al., 1989. Effective elastic plate thickness beneath the East African and Afar plateaus and dynamic compensation of the uplifts. Journal of Geophysical Research: Solid Earth 94, 2883-2901.

Flament, N., et al., 2013. A review of observations and models of dynamic topography. Lithosphere 5, 189-210.

Forsyth, D., Uyeda, S., 1975. On the Relative Importance of the Driving Forces of Plate Motion. Geophysical Journal of the Royal Astronomical Society 43, 163-200.

Forsyth, D.W., 1985. Subsurface loading and estimates of the flexural rigidity of continental lithosphere. Journal of Geophysical Research: Solid Earth 90, 12623-12632.

Gvirtzman, Z., et al., 2016. Isostasy, flexure, and dynamic topography. Tectonophysics 683, 255-271.

Hall, C.E., et al., 2003. Catastrophic initiation of subduction following forced convergence across fracture zones. Earth and Planetary Science Letters 212, 15-30.

Hall, R., 1996. Reconstructing Cenozoic SE Asia. Geological Society, London, Special Publications 106, 153-184.

Hall, R., 2002. Cenozoic geological and plate tectonic evolution of SE Asia and the SW Pacific: computer-based reconstructions, model and animations. Journal of Asian Earth Sciences 20, 353-431.

Heine, C., et al., 2008. Subsidence in intracontinental basins due to dynamic topography. Physics of the Earth and Planetary Interiors 171, 252-264.

Hilde, T.W.C., et al., 1977. Present State of Plate Tectonics Evolution of the western pacific and its margin. Tectonophysics 38, 145-165.

Honza, E., Fujioka, K., 2004. Formation of arcs and backarc basins inferred from the tectonic evolution of Southeast Asia since the Late Cretaceous.

Tectonophysics 384, 23-53.

Hunter, J., Watts, A.B., 2016. Gravity anomalies, flexure and mantle rheology seaward of circum-Pacific trenches. Geophysical Journal International 207, 288-316.

Husson, L., 2006. Dynamic topography above retreating subduction zones. Geology 34, 741-744.

IOC, I., BODC,, 2003. Centenary edition of the GEBCO Digital Atlas, published on behalf of the Intergovernmental Oceanographic Commission and the International Hydrographic Organization as part of the General Bathymetric Chart of the Oceans, in: Centre, B.O.D. (Ed.), Liverpool, U.K.

Isaak, D.G., et al., 1989. Elasticity of single-crystal forsterite measured to 1700 K. Journal of Geophysical Research: Solid Earth 94, 5895-5906.

Jolivet, L., et al., 1989. Subduction Zones: The Kaiko Project Tectonic setting of Western Pacific marginal basins. Tectonophysics 160, 23-47.

Kalnins, L.M., Watts, A.B., 2009. Spatial variations in effective elastic thickness in the Western Pacific Ocean and their implications for Mesozoic volcanism. Earth and Planetary Science Letters 286, 89-100.

Karato, S.-i., 1993. Importance of anelasticity in the interpretation of seismic tomography. Geophysical Research Letters 20, 1623-1626.

Karato, S.-i., Karki, B.B., 2001. Origin of lateral variation of seismic wave velocities and density in the deep mantle. Journal of Geophysical Research 106, 21771-21783.

Kirby, J.F., 2005. Which wavelet best reproduces the Fourier power spectrum? Computers & Geosciences 31, 846-864.

Kirby, J.F., 2014. Estimation of the effective elastic thickness of the lithosphere using inverse spectral methods: The state of the art. Tectonophysics 631, 87-116.

Kirby, J.F., Swain, C.J., 2004. Global and local isostatic coherence from the wavelet transform. Geophysical research letters 31, L24608.

Kirby, J.F., Swain, C.J., 2008. An accuracy assessment of the fan wavelet coherence method for elastic thickness estimation. Geochemistry, Geophysics, Geosystems 9, Q03022.

Kirby, J.F., Swain, C.J., 2011. Improving the spatial resolution of effective elastic thickness estimation with the fanwavelet transform. Computers &Geosciences 37, 1345-1354.

Kirby, J.F., Swain, C.J., 2013. Power spectral estimates using two-dimensional Morlet-fan wavelets with emphasis on the long wavelengths: jackknife errors, bandwidth resolution and orthogonality properties. Geophysical Journal International 194, 78-99.

Kong, X., et al., 2018. Causes of earthquake spatial distribution beneath the

Izu-Bonin-Mariana Arc. Journal of Asian Earth Sciences 151, 90-100.

Müller, R.D., et al., 2008. Age, spreading rates, and spreading asymmetry of the world's ocean crust. Geochemistry, Geophysics, Geosystems 9, Q04006.

Macario, A., et al., 1995. On the robustness of elastic thickness estimates obtained using the coherence method. Journal of Geophysical Research: Solid Earth 100, 15163-15172.

Mason, W.G., et al., 2010. Three-dimensional numerical models of the influence of a buoyant oceanic plateau on subduction zones. Tectonophysics 483, 71-79.

McKenzie, D., Fairhead, D., 1997. Estimates of the effective elastic thickness of the continental lithosphere from Bouguer and free air gravity anomalies. Journal of Geophysical Research: Solid Earth 102, 27523-27552.

McNutt, M.K., Menard, H.W., 1982. Constraints on yield strength in the oceanic lithosphere derived from observations of flexure. Geophys J Int 71, 363-394.

Morgan, W.J., 1965. Gravity anomalies and convection currents: 1. A sphere and cylinder sinking beneath the surface of a viscous fluid. Journal of Geophysical Research 70, 6175-6187.

Niu, Y., 2014. Geological understanding of plate tectonics: Basic concepts, illustrations, examples and new perspectives. Global Tectonics and Metallogeny 10, 23-46.

Oldenburg, D., 1974. The inversion and interpretation of gravity anomalies. Geophysics 39, 526-536.

Oruç, B., Sönmez, T., 2017. The rheological structure of the lithosphere in the Eastern Marmara region, Turkey. Journal of Asian Earth Sciences 139, 183-191.

Pérez-Gussinyé, M., et al., 2008. Effective elastic thickness variations along the Andean margin and their relationship to subduction geometry. Geochemistry, Geophysics, Geosystems 9, Q02003.

Pérez-Gussinyé, M., et al., 2004. On the recovery of effective elastic thickness using spectral methods: Examples from synthetic data and from the Fennoscandian Shield. Journal of Geophysical Research: Solid Earth 109, B10409.

Parker, R.L., 1973. The Rapid Calculation of Potential Anomalies. Geophysical Journal International 31, 447-455.

Press, W.H., et al., 1992. Numerical Recipes in Fortran 77, Second ed. Cambridge University Press, Cambridge.

Ratheesh Kumar, R.T., et al., 2013. Elastic thickness structure of the Andaman subduction zone: Implications for convergence of the Ninetyeast Ridge. Journal of Asian Earth Sciences 78, 291-300.

Schaeffer, A.J., Lebedev, S., 2013. Global shear speed structure of the upper mantle and transition zone. Geophysical Journal International 194, 417-449.

Sdrolias, M., et al., 2004. An expression of Philippine Sea plate rotation: the Parece Vela and Shikoku Basins. Tectonophysics 394, 69-86.

Shi, X., et al., 2017. Spatial variations in the effective elastic thickness of the lithosphere in Southeast Asia. Gondwana Research 42, 49-62.

Simons, F.J., Olhede, S.C., 2013. Maximum-likelihood estimation of lithospheric flexural rigidity, initial-loading fraction and load correlation, under isotropy. Geophysical Journal International 193, 1300-1342.

Simons, F.J., et al., 2000. Isostatic response of the Australian lithosphere: Estimation of effective elastic thickness and anisotropy using multitaper spectral analysis. Journal of Geophysical Research: Solid Earth 105, 19163-19184.

Smith, W.H.F., Sandwell, D.T., 1994. Bathymetric prediction from dense satellite altimetry and sparse shipboard bathymetry. Journal of Geophysical Research: Solid Earth 99, 21803-21824.

Steinberger, B., 2007. Effects of latent heat release at phase boundaries on flow in the Earth's mantle, phase boundary topography and dynamic topography at the Earth's surface. Physics of the Earth and Planetary Interiors 164, 2-20.

Stern, R.J., et al., 2004. An Overview of the Izu-Bonin-Mariana Subduction Factory, Inside the Subduction Factory. American Geophysical Union, pp. 175-222.

Swain, C.J., Kirby, J.F., 2006. An effective elastic thickness map of Australia from wavelet transforms of gravity and topography using Forsyth's method. Geophysical Research Letters 33, L02314.

Thomson, D.J., Chave, A.D., 1991. Jackknifed error estimates for spectra, coherences, and transfer functions. Prentice Hall, Englewood Cliffs, N.J.

Walcott, R.I., 1970. Flexural rigidity, thickness, and viscosity of the lithosphere. Journal of Geophysical Research 75, 3941-3954.

Watts, A.B., et al., 1980. Observations of flexure and the state of stress in the oceanic lithosphere. Journal of Geophysical Research: Solid Earth 85, 6369-6376.

Zhang, B., et al., 2016. Docking and subduction of the West Pacific seamounts along the Mariana Trench and their effects. Geological Journal 51, 579-592.

Zhang, F., et al., 2014. Variations in oceanic plate bending along the Mariana trench. Earth and Planetary Science Letters 401, 206-214.

Zhong, S., Gurnis, M., 1994. Controls on trench topography from dynamic models of subducted slabs. Journal of Geophysical Research: Solid Earth 99, 15683-15695.

Table 1 Physical constants for T_e estimation after Ratheesh Kumar et al. (2013)

Constant	symbol	value	Unit
Young modulus	E	10^{11}	Pa
Newtonian gravitational constant	G	6.67×10^{-11}	$m^3 kg^{-1} s^{-2}$
Poisson ratio	ν	0.25	
gravitational acceleration	g	9.81	m/s^2
seawater density	ρ_w	1030	kg/m^3
basement density	ρ_b	2800	kg/m^3
mantle density	ρ_m	3300	kg/m^3

FIGURES

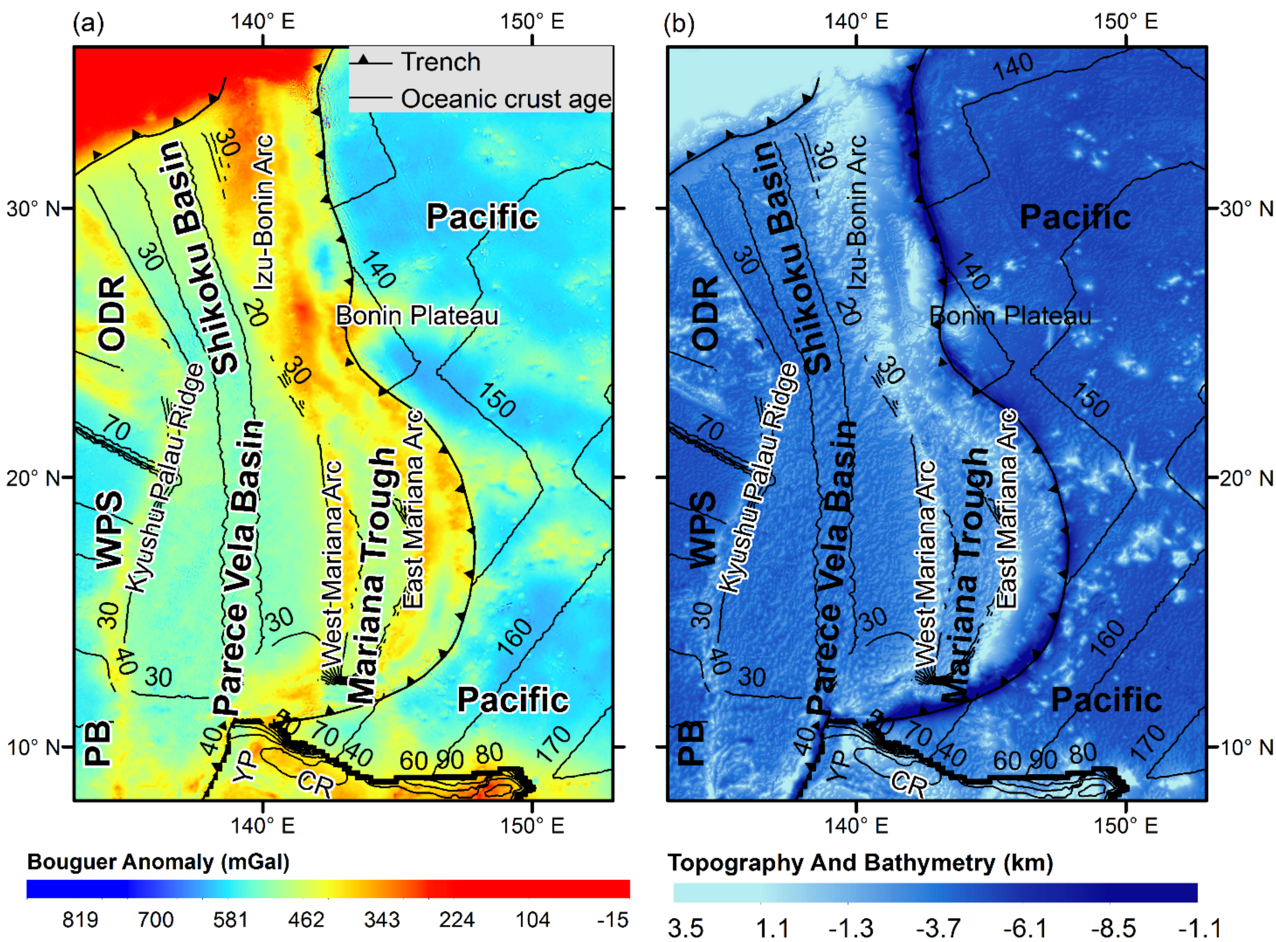

Figure 1. (a) The Bouguer gravity anomaly from the Bureau Gravimétrique International (Balmino et al., 2012), and (b) the topography and bathymetry from ETOPO1 (Amante and Eakins, 2009), of the IBM subduction system and surroundings. The oceanic crustal age contour (labelled in m.y.) is based on the age grid provided by Müller et al. (2008). Abbreviations: WPS, West Philippine Sea; ODR, Oki-Daito Ridge; PB, Palau Basin; YT, Yap Trench; CR, Caroline Ridge.

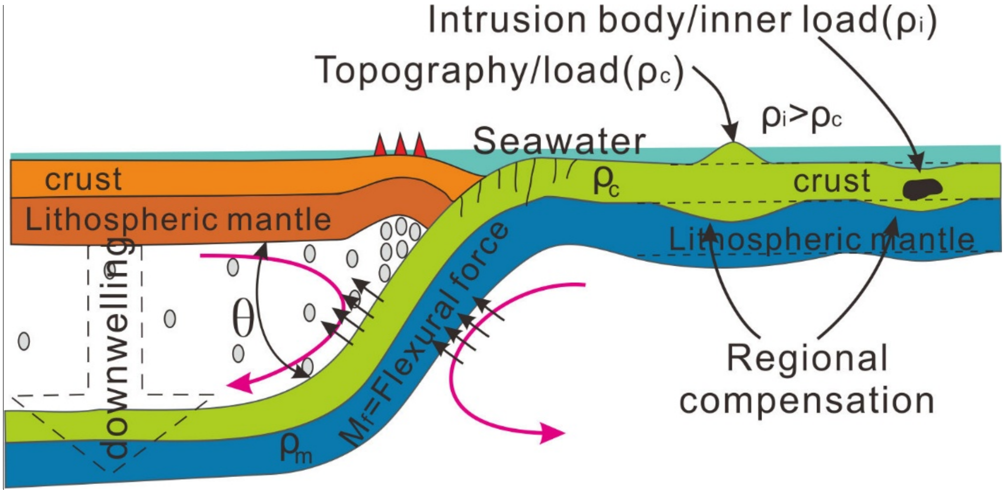

Figure 2. Cartoon showing compensation mode and subduction dynamics. The dashed lines represent the initial topography, Moho and lithospheric bottom. Subsequent magmatic intrusion and mountain formation results in lithospheric bending and compensation surface adjustment. Viscous asthenosphere transmits the dynamic forces due to slab sinking to the overlying plate and induces topography changes. Water released from dehydration of the subducted slab results in lithospheric partial melting and reduction of lithospheric strength (Chen et al., 2013). Pink arrows represent mantle flow at different locations (Pérez-Gussinyé et al., 2008). θ is the subduction angle.

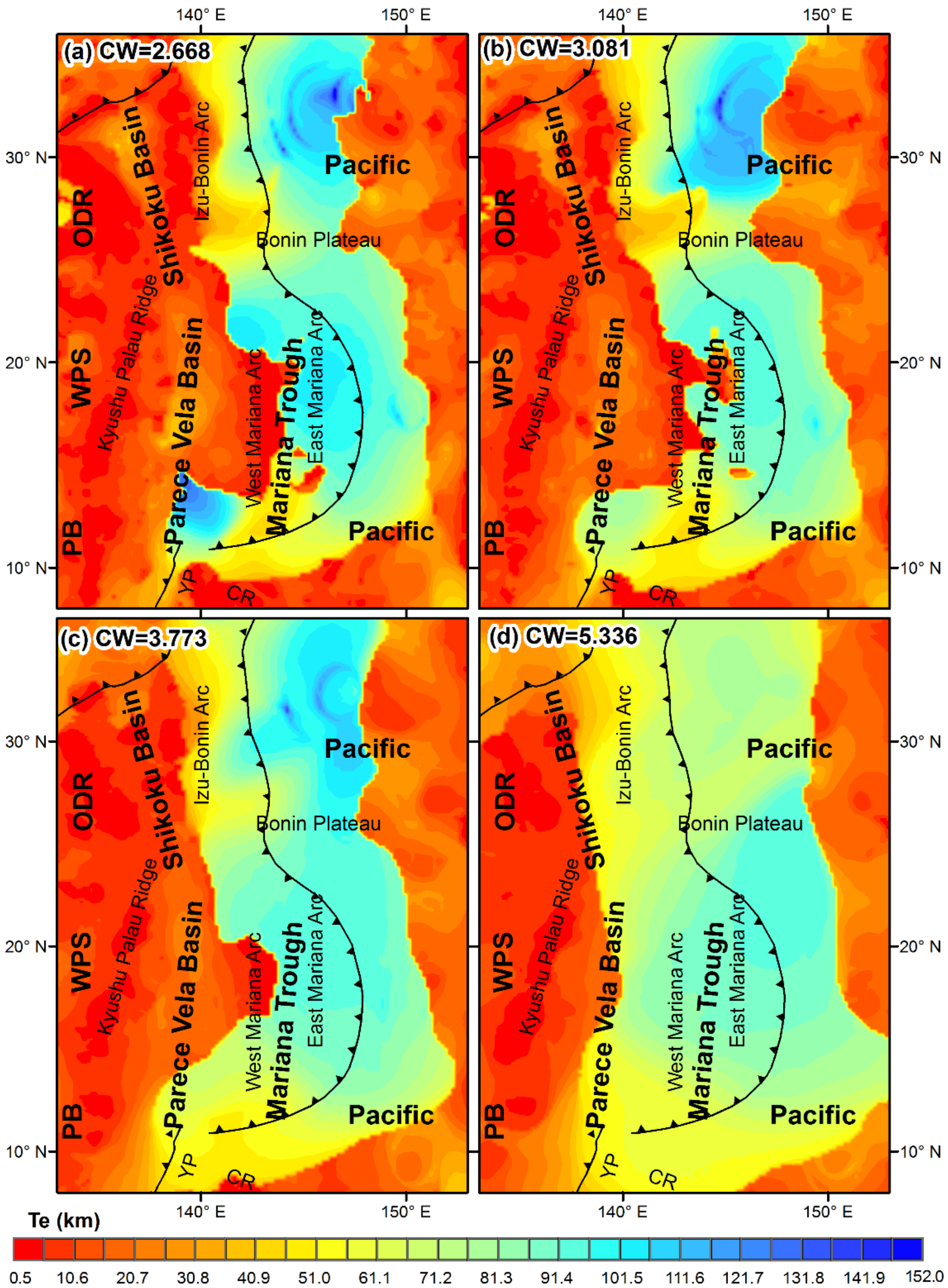

Figure 3. T_e estimation results (without slab corrections) based on four different central wavenumber (CW) values. Abbreviations can be found in the caption to Figure 1.

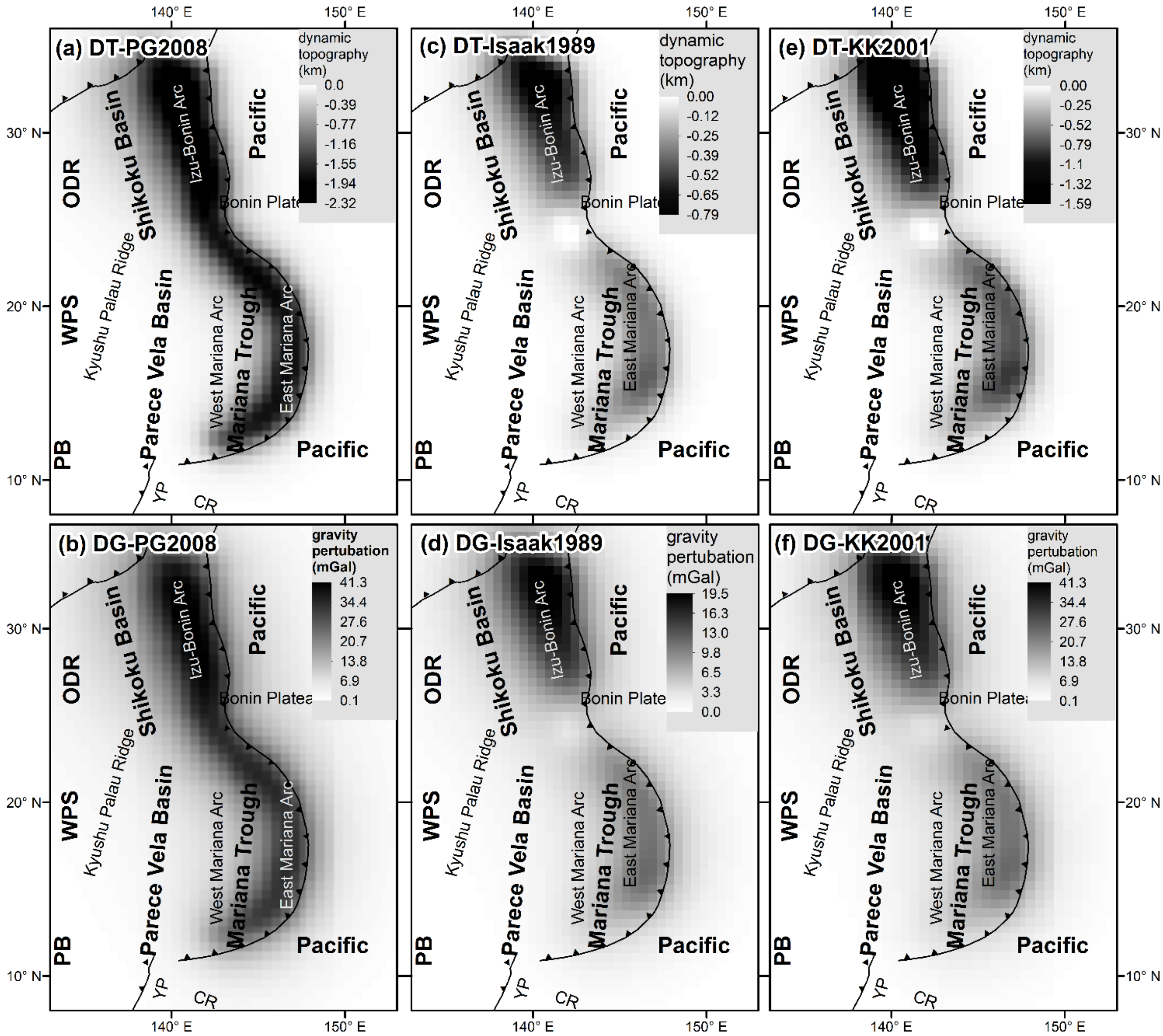

Figure 4. Dynamic topography (DT) on the top panels and dynamic gravity (DG) on the bottom panels induced by the sinking of the subducted Pacific plate when the slab density is based on the PG2008, Isaak1989 and KK2001 methods, respectively. See Figure 1 for abbreviations.

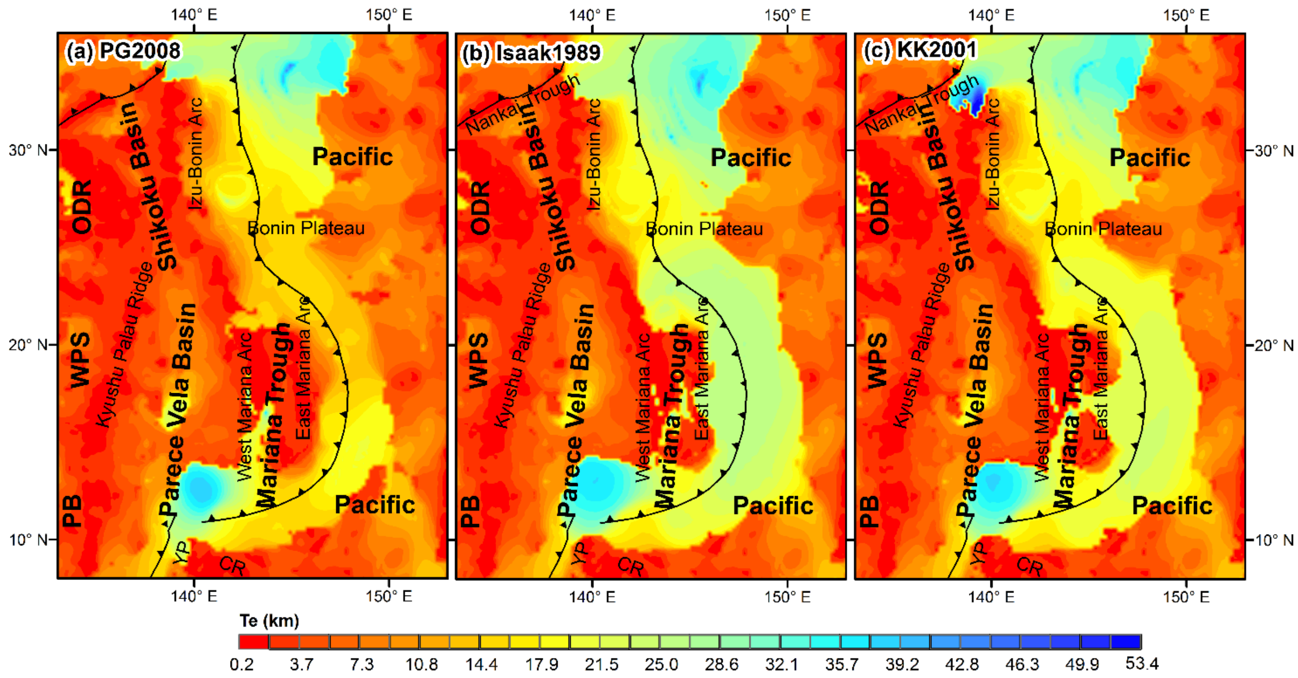

Figure 5. T_e maps using residual gravity and topography, when the subducted slab density is modelled using the PG2008, Isaak1989 and KK2001 methods, respectively (central wavenumber is 2.668 in all). Abbreviations are the same as Figure 1.

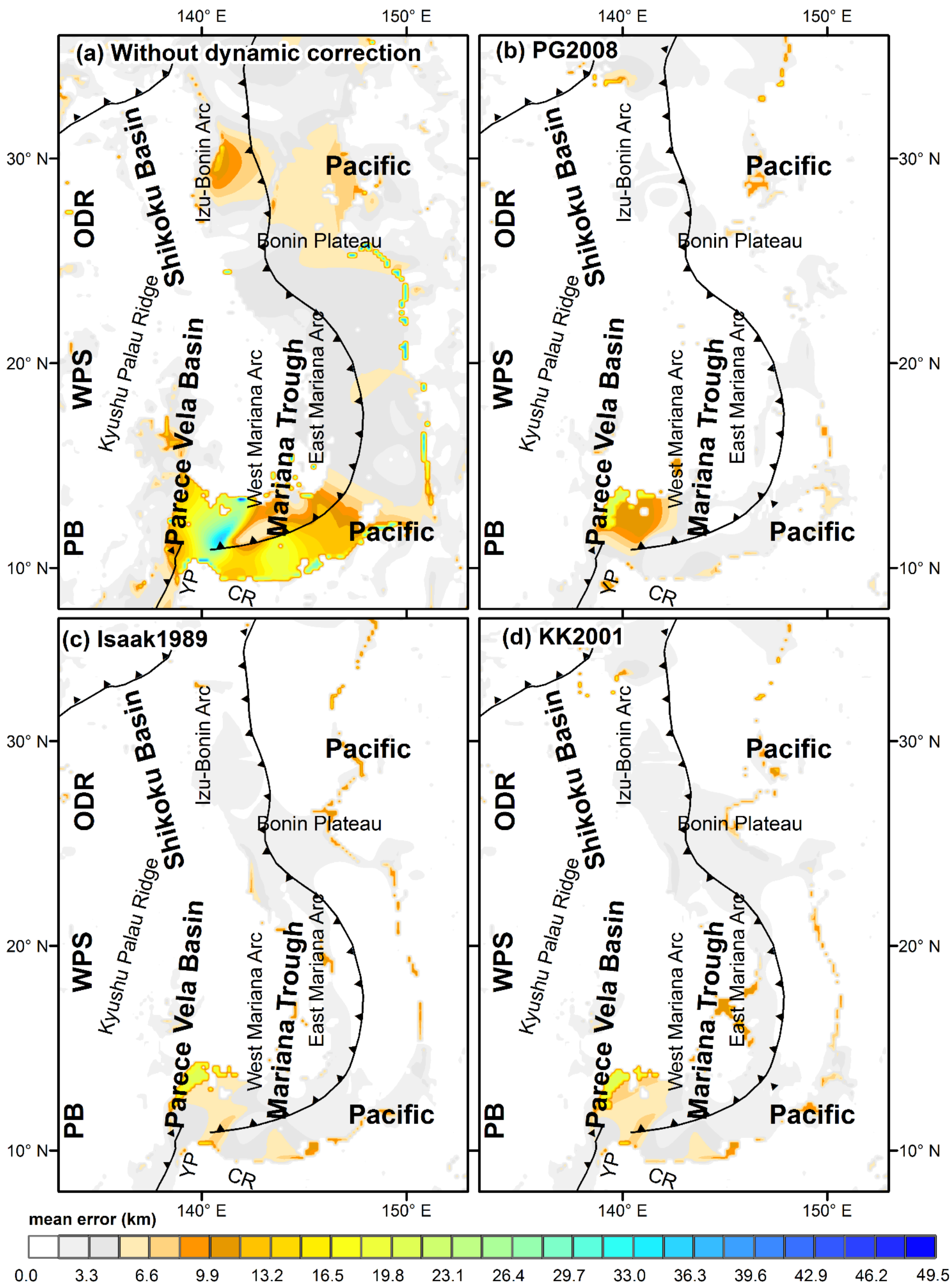

Figure 6. T_e error maps (a) without dynamic corrections to the gravity and topography data, and when dynamic corrections are based on the (b) PG2008, (c) Isaak 1989, and (d) KK2001 methods, respectively. The central wavenumber for all maps is 2.668.

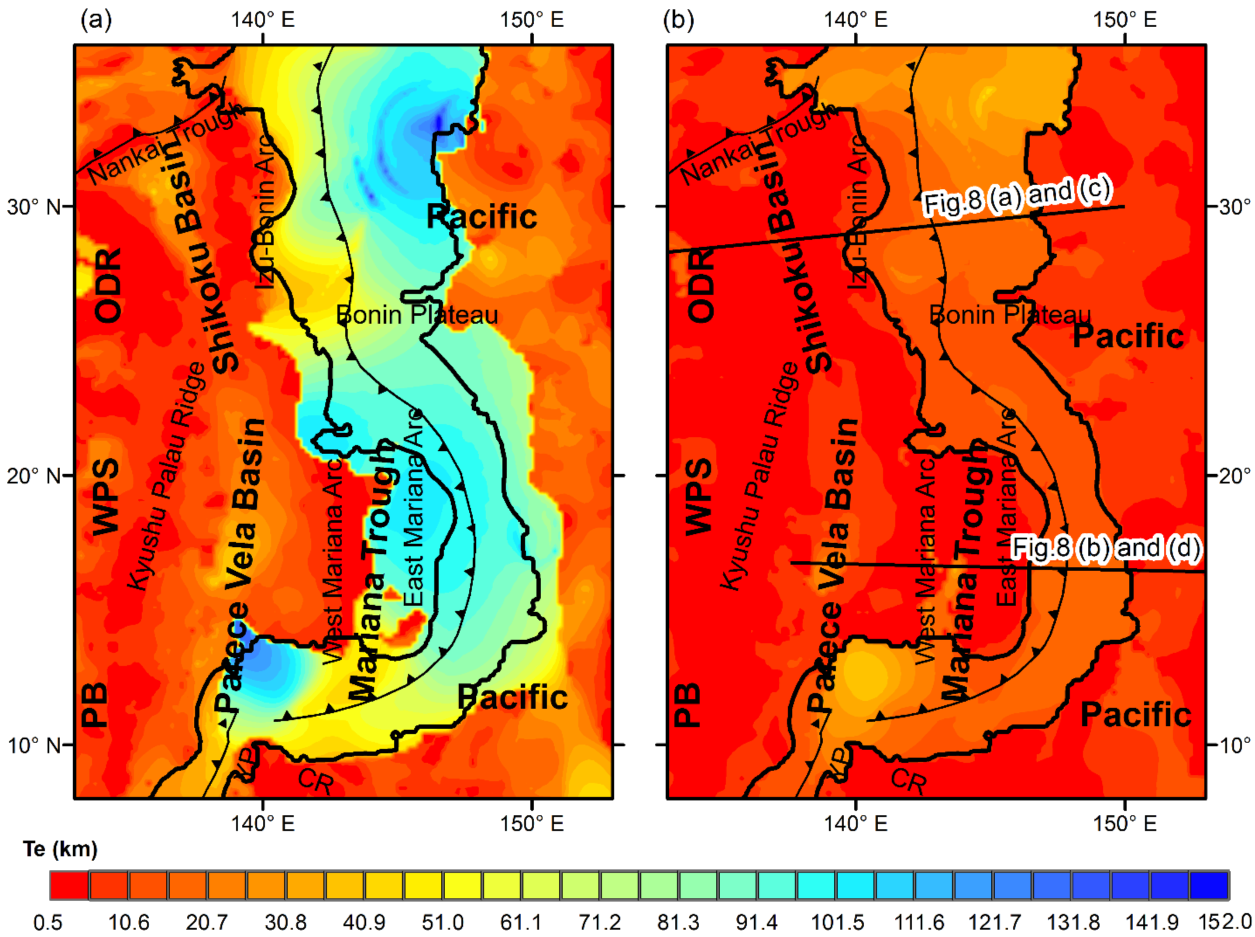

Figure 7. T_e maps (a) before and (b) after considering the influence of pull-force by the subducted slab of the Pacific plate on topography and gravity (CW = 2.668). The solid black lines in (a) and (b) are the outer boundaries of the high-T_e band from Figure 5b. (a) is a reproduction of Figure 3a, while (b) is a reproduction of Figure 5b. All abbreviations are the same as Figure 1.

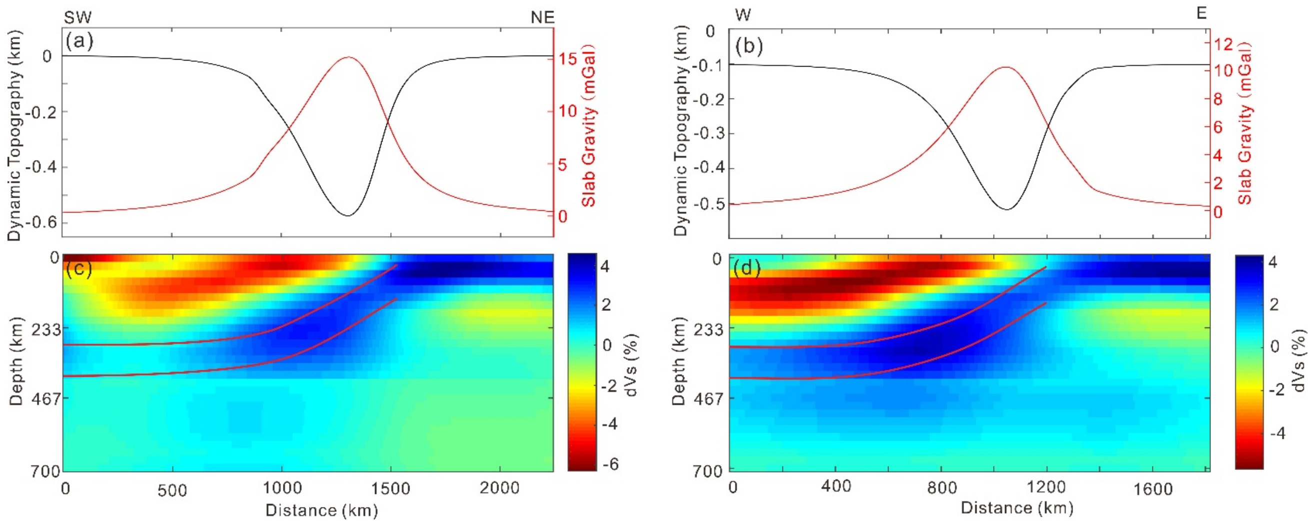

Figure 8. Two profiles show seismic velocity structure (on bottom panel), dynamic topography and slab gravity (black and right curve respectively on top panel). Slab density modelling is based on the Isaak1989 method for dynamic effect calculations. The red curves on the bottom show the slab geometries with 100 km thickens. The profile locations are shown in Figure 7.